inorganics

MDPI

Article

Sub-Ambient Fast Magnesium Ionic Conductivity in Diethylamine Magnesium Tetrahydridoborate and Its Crystal Structure

Oliver G. Ørtoft, Lasse R. Kristensen and Torben R. Jensen *

Interdisciplinary Nanoscience Center (iNANO) and Department of Chemistry, Aarhus University, Langelandsgade 140, 8000 Aarhus C, Denmark
* Correspondence: trj@chem.au.dk

Abstract

Magnesium tetrahydridoborate derivatives are promising electrolytes for next-generation solid-state batteries due to their high Mg^{2+} conductivity and stability towards magnesium metal. Here, we report the synthesis, crystal structure and thermal properties of mono-diethylamine magnesium tetrahydridoborate, $Mg(BH_4)_2{\cdot}NH(CH_2CH_3)_2$, and the ionic conductivity of the composite $Mg(BH_4)_2{\cdot}NH(CH_2CH_3)_2$−60wt% Al_2O_3. Synchrotron radiation powder X-ray diffraction data combined with ab initio structure determination and density functional theory reveal a monoclinic structure ($P2_1/c$) comprising one-dimensional zig-zag chains interconnected by dihydrogen bonds and dispersive interactions between organic moieties ($–CH_2CH_3$). The compound melts at 83 °C and begins to decompose at 116 °C. Owing to their soft and malleable nature, 60wt% Al_2O_3 nanoparticles (13 nm) were incorporated to provide mechanical stability, which stabilizes the soft electrolyte while preserving thermal stability. Electrochemical impedance spectroscopy of the composite $Mg(BH_4)_2{\cdot}NH(CH_2CH_3)_2$−60wt% Al_2O_3 demonstrates exceptionally high ionic conductivity, reaching $\sigma = 2.58 \times 10^{-6}$ S cm^{-1} at −2 °C and crossing 10^{-4} S cm^{-1} below 40 °C with an activation energy of 695 ± 11 meV, representing one of the highest conductivities reported for a magnesium hydridoborate derivative. The conductivity decreases significantly when heated above 40 °C, suggesting that slow drying is occurring. This is supported by a decrease in conductivity upon long-term storage. These results highlight the potential of ligand-mediated structural flexibility in enabling highly conductive magnesium solid electrolytes for near room-temperature solid-state inorganic batteries.

Keywords: magnesium solid-state electrolyte; ionic conductivity; crystal structure; inorganic synthesis; hydridoborate; thermal analysis; structural flexibility

Check for updates

Academic Editor: Yuping Wu

Received: 17 September 2026
Revised: 22 October 2026
Accepted: 28 October 2026
Published: 29 October 2026

Copyright: © 2026 by the authors. Licensee MDPI, Basel, Switzerland. This article is an open access article distributed under the terms and conditions of the Creative Commons Attribution (CC BY) license.

1. Introduction

Batteries enable efficient utilization of intermittent renewable energy sources, such as solar and wind power, which enables a sustainable future [1–4]. Most batteries today are based on the limited resource lithium, which poses a significant concern due to the continual increase in demand. Moving away from lithium is challenging due to difficulties in reaching high energy densities and performance similar to lithium-ion battery technologies. One avenue is to exchange the low-capacity intercalation anodes, such as graphite, with pure metals. Looking solely at achieving maximum energy density, magnesium metal stands out due to its high volumetric capacity (3833 mAh cm^{-3}) [5]. This is significantly higher than both graphite (873 mAh cm^{-3}) and lithium metal (2062 mAh cm^{-3}) [6]. Combining this with a sulphur cathode has the potential to enable ultra-high-energy-density batteries

of more than 3200 Wh L^{-1} [7,8]. However, magnesium sulphur batteries are notorious for having issues with sulphur 'shuttling', causing continuous SEI formation owing to dissolution of sulphur in the organic liquid electrolytes [9,10]. To resolve this challenge, electrolytes with high ionic selectivity are needed, which is an intrinsic characteristic of solid-state electrolytes. However, this property needs to be combined with very high cationic conductivity, which is a challenge as the selectivity arises from the challenge of conducting ions in the solid state, requiring very specific structural design [11,12]. Furthermore, magnesium is burdened by being a divalent cation, resulting in stronger interaction with the anion lattice, which lowers the overall Mg^{2+} conductivity [12]. In recent years, magnesium hydridoborate derivatives have achieved fast magnesium ionic conductivity at near ambient conditions [13–17].

Magnesium tetrahydridoborate, $Mg(BH_4)_2$, is an electronic and ionic insulator at room temperature due to a 3D structural network without redox-active atoms [18,19]. Furthermore, the tetrahydridoborate (BH_4^-) anion is stable towards magnesium metal, lowering solid electrolyte interface formation [20]. In 2017, Roedern et al. showed that solid-state ionic conductivity of $Mg(BH_4)_2$ can be increased by several orders of magnitude by the addition of stoichiometric quantities of the neutral molecule ethylenediamine (1–2 molecules per formula unit) [21]. The neutral molecule coordinates to magnesium through the nitrogen lone pair, which opens the crystal structure and thereby facilitates ionic conductivity [22]. Since then, a variety of new compounds and composites have been discovered, each pushing the cationic conductivity higher and higher [13–17,23,24]. Through this work, three main trends have been discovered. First, optimal conductivity is reached at a ligand content between 1 and 2 per formula unit [14,15]. Second, mixing different crystalline compounds with similar compositions tends to increase ionic conductivity while also lowering the overall melting point [25,26]. Third, neutral molecules that consist of polar and apolar moieties tend to have higher conductivities and low activation energies [13,27]. On this final point, the improved cation mobility is attributed to the presence of apolar regions with weak dispersion interactions that increase overall structural flexibility [28]. Introducing the anion NH_2^- also increases conductivity, but to a lesser extent than is observed for anion mixing in other metal hydridoborate systems [24,29–33].

Magnesium hydridoborate readily reacts with a variety of neutral molecules to form complex structures and is considered saturated when magnesium is solely coordinated by the neutral molecules and the tetrahydridoborate anions act as counterions, usually in an octahedral geometry [13,34]. However, for larger molecules such as pyridine and isopropylamine, a lower maximum ligand content can be obtained, likely due to steric hindrance [14,27]. The ligand content can be tuned through drying and mechanochemical methods, giving access to a larger variety of compounds with different crystal structures and magnesium conductivities.

Metal tetrahydridoborates have a range of prolific properties as electrolytes for solid-state batteries [19]. They are built from a combination of covalent and ionic bonding and weak interactions such as dihydrogen bonding, $B–H^{\delta-}\cdots{}^{+\delta}H–N$, and dispersion interactions between organic moieties and therefore have intrinsic 'zero' electronic conductivity. They are also compatible with a range of oxides, sulphides and halides, which allow the utilization of known cathode materials. The tetrahydridoborate complex forms cationic conducting interphases to high-voltage cathodes by oxidation to form *closo*-borates and their dimers and trimers [35–37]. They also have (kinetic) stability towards metallic anodes such as Li, Na, Ca and Mg [38–44]. Furthermore, excellent plating and stripping characteristics have been reported in both liquid and solid-state systems [16,42,45–51].

Here we present the synthesis of mono-diethylamine magnesium tetrahydridoborate, which has a 1D chain-like structure held together by a combination of ionic bonds, di-

hydrogen bonds and dispersion interactions. The structure is solved from synchrotron radiation powder X-ray diffraction data using ab initio methods and verified by density functional theory. The compound is found to have high ionic conductivity at room temperature by electrochemical impedance spectroscopy, while also having relatively high thermal stability determined by a combination of thermogravimetric analysis and differential scanning calorimetry.

2. Results and Discussion

2.1. Synthesis and Chemical Characterization

Mono-diethylamine magnesium tetrahydridoborate, $Mg(BH_4)_2{\cdot}NH(CH_2CH_3)_2$, was synthesized via a gas–solid reaction using specially developed glassware (see Figure 1). The reaction product was a sticky solid denoted as sample S1. This material was mechanically stabilized using aluminum oxide (Al_2O_3) nanoparticles (60 wt%, 13 nm), which were added and ground by hand (mortar and pestle) to form a homogeneous sample (S2). Mechanochemical treatment (ball milling) was also attempted to form sample S3. A summary of the samples is provided in Table 1.

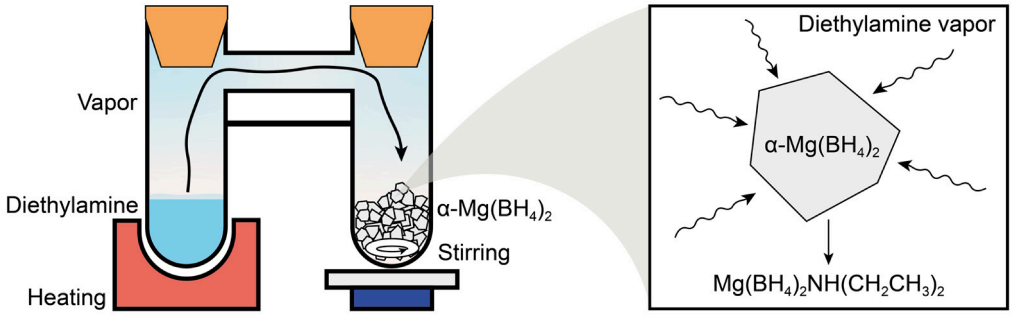


Figure 1. Gas-mediated coordination of diethylamine. One chamber containing diethylamine was heated gently to increase the vapor pressure. This allows for a controlled reaction between $Mg(BH_4)_2$ and diethylamine. Stirring of the powder is used to increase sample homogeneity of the product.

Table 1. Compositions of samples S1–S3 and addition amounts and methods of Al_2O_3 nanoparticles.

Sample	Composition	Al_2O_3 Content and Addition Method
S1	$Mg(BH_4)_2{\cdot}0.96(\pm0.07)NH(CH_2CH_3)_2$	-
S2	$Mg(BH_4)_2{\cdot}0.87(\pm0.06)NH(CH_2CH_3)_2$	60 wt% (by hand)
S3	Significantly decomposed	70 wt% (ball milling)

Fourier transform infrared spectroscopy (FT-IR) of S1 and S2 shows a clear change in B-H bonding modes as diethylamine is introduced to α-$Mg(BH_4)_2$ (Figure 2a). Here, one unique boron environment is present in α-$Mg(BH_4)_2$, whereas S1 and S2 show three different bending modes. Vibrational modes of C-H are also detected, suggesting that diethylamine is present in the sample. Powder X-ray diffraction of S1 shows a clear evolution from α-$Mg(BH_4)_2$ with no overlap between the patterns, suggesting a complete reaction to a crystalline product (see Figure 2b).

Liquid-state ^{1}H-NMR and ^{11}B-NMR before (S1) and after (S2) addition of Al_2O_3 nanoparticles by hand using a mortar and pestle show compositions of $Mg(BH_4)_2{\cdot}0.96(\pm0.07)NH(CH_2CH_3)_2$ and $Mg(BH_4)_2{\cdot}0.87(\pm0.06)NH(CH_2CH_3)_2$, respectively (see Figure S1). Ligand contents were determined through liquid-state ^{1}H-NMR using [BH_4^-] as a hydrogen content reference, which was calibrated through a diethylamine relaxation experiment (see Figure S2). A slight decrease in diethylamine content was detected after addition of Al_2O_3 nanoparticles; however, this is within the standard deviation.

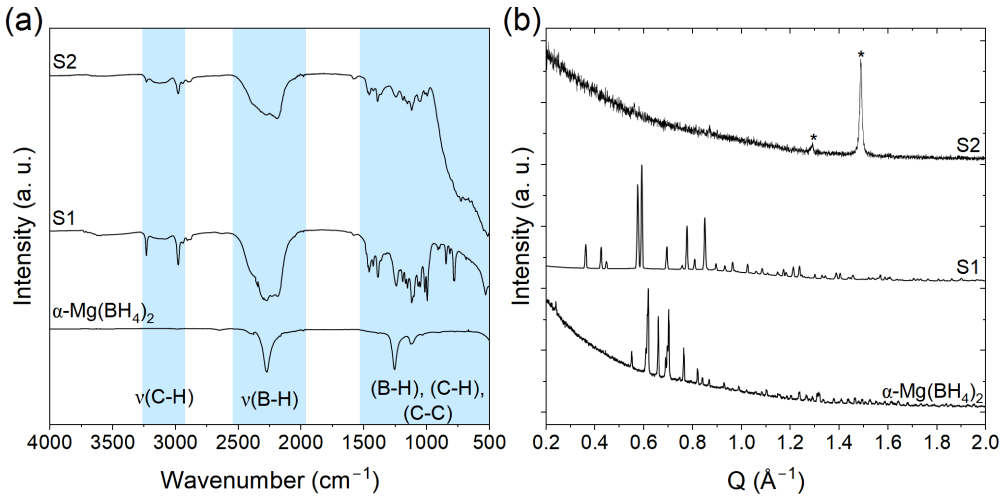


Figure 2. Initial characterization of samples. (**a**) FT-IR spectra and (**b**) powder X-ray diffraction patterns of samples S1, S2 and α-$Mg(BH_4)_2$. The diffraction patterns of α-$Mg(BH_4)_2$ and S2 were collected using an in-house diffractometer equipped with a monochromatic copper source (λ = 1.54056 Å), whereas data on S1 were collected at MAXIV in Lund, Sweden, using synchrotron radiation (λ = 0.61992 Å) at room temperature. Bragg peaks of Al_2O_3 are marked with (*).

A decomposition of the [BH_4^-] anion was detected in the ^{11}B-NMR measurement for the initial sample (S1) as well as for the mechanically stabilized sample (S2). However, the decomposition level did not change after the addition of Al_2O_3 nanoparticles. A significant decomposition of the [BH_4^-] anion was detected in a secondary sample (S3) after ball milling, which indicates that the mechano-chemical treatment facilitates the decomposition of the composite (see Figure S3).

2.2. Crystal Structure of $Mg(BH_4)_2{\cdot}NH(CH_2CH_3)_2$

The crystal structure of $Mg(BH_4)_2{\cdot}NH(CH_2CH_3)_2$ was indexed in the monoclinic space group $P2_1/c$ with unit cell parameters a = 8.700(3), b = 14.097(6), c = 8.099(3) Å, β = 90.36(3)° and V = 993.31(7) Å^3 at T = 22 °C, see Figure 3 (CCDC: 2592034). The structure shares the same 1-D alternating BH_4-Mg-BH_4 chain structure-type as observed for $Mg(BH_4)_2{\cdot}NH_2CH_3$, $Mg(BH_4)_2{\cdot}NH_3$, $Mg(BH_4)_2{\cdot}NH_2CH(CH_3)_2$ and the solid solution $Mg(BH_4)_2{\cdot}(NH_3)_{1-x}(CH_3NH_2)_x$ (see Figure 3a) [13,26,52,53]. The chains and ligands form alternating layers of polar and apolar moieties, showing that the layers are held together by dispersion interactions in the *a*-direction (see Figure 3b), while chains are held together by strong hydrogen bonding with a bond length of approx. 2.1 Å (see Figure 3c). The coordination environment of Mg^{2+} is a slightly distorted tetrahedra, [$Mg(BH_4)_2NH(CH_2CH_3)_2$] (see Figure 3d), where $NH(CH_2CH_3)_2$ coordinates Mg^{2+} through the lone pair on N, one [BH_4^-] is terminal (κ^3), and the other two [BH_4^-] form the chain (κ^2). This tetrahedral distortion of [$Mg(BH_4)_3NH(CH_2CH_3)_2$] observed in the structure of $Mg(BH_4)_2NH(CH_2CH_3)_2$ is lower than the similar systems $Mg(BH_4)_2NH_3$ and $Mg(BH_4)_2NH_2CH_3$ at a root-mean-square (RMS) angular deviation of only 1.81° from the ideal tetrahedral angle of 109.47° whereas this value is 4.96° and 5.81° for $Mg(BH_4)_2NH_3$ and $Mg(BH_4)_2NH_2CH_3$, respectively [13,53]. This is somewhat unexpected due to the bulk of the ligand and suggests that the structural motif may accommodate even larger molecules. The structural model is in good agreement with synchrotron radiation powder X-ray diffraction data (see Figure 4) and contains multiple B−H environments, which is consistent with FT-IR data shown in Figure 2a and similar structures [13,26,52,53]. Upon refinement, the structure contorts slightly; however, the overall connectivity of the structure is maintained (Figure S4).

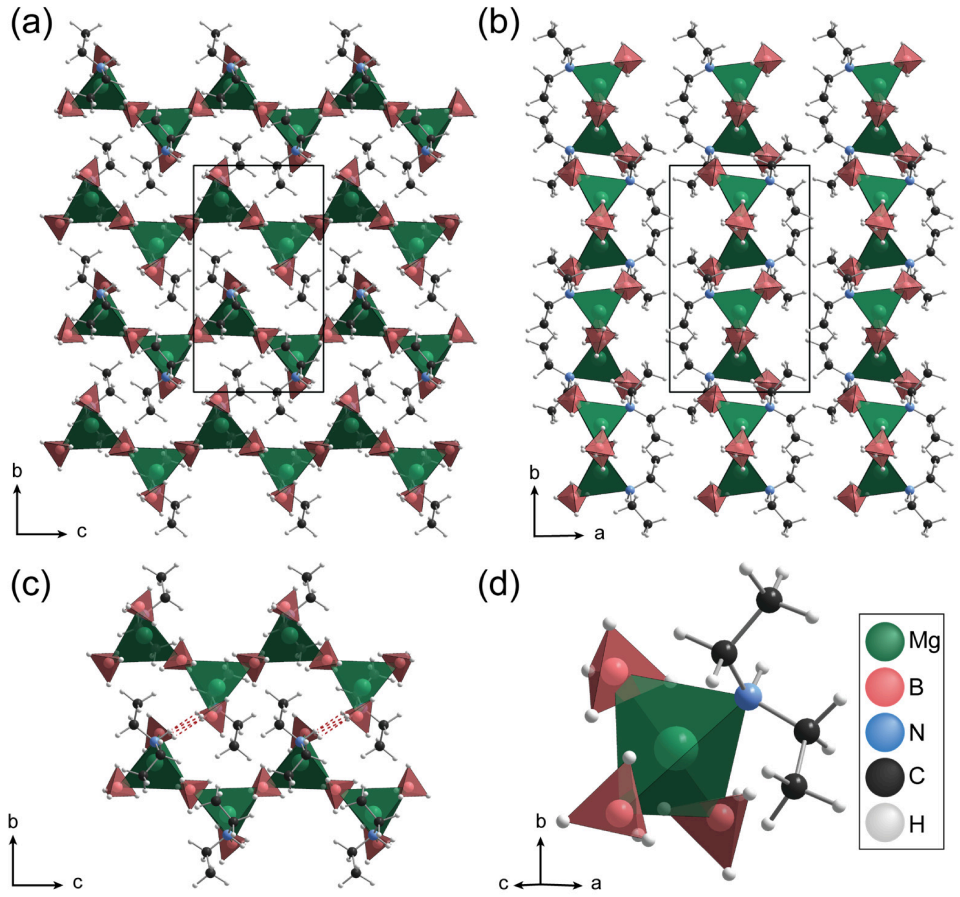


Figure 3. DFT-optimized crystal structure of $Mg(BH_4)_2{\cdot}NH(CH_2CH_3)_2$. (**a**) View along the *a*-direction showing chain-like structure. (**b**) View along the *c*-direction showing the alternating polar and apolar layers within the structure. (**c**) Hydrogen bonding between $N{-}H^{\delta+}\cdots{}^{-\delta}H{-}B$ moieties belonging to different chains. (**d**) Local coordination environment of Mg^{2+}.

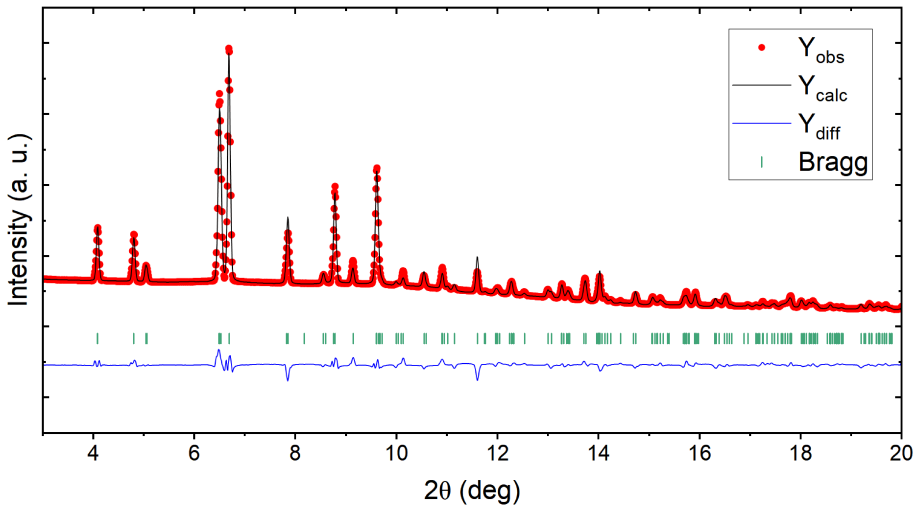


Figure 4. Structural refinement of the $Mg(BH_4)_2{\cdot}NH(CH_2CH_3)_2$ structure using synchrotron radiation powder X-ray diffraction data. Synchrotron radiation powder X-ray diffraction data (red, $\lambda = 0.61992$ Å), calculated diffraction pattern from Rietveld refinement of the $Mg(BH_4)_2{\cdot}NH(CH_2CH_3)_2$ structural model (black), difference between data and model (blue), and Bragg peaks of $P2_1/c$. The diffraction pattern was measured at 22 °C. Final reliability factors with all non-excluded points: $R_p = 2.81\%$, $R_{wp} = 4.30\%$ (not corrected for background), $R_p = 17.7\%$, $R_{wp} = 15.8\%$ (conventional Rietveld R-factors), $R_{Bragg} = 8.97$ and global $\chi^2 = 2.01$. Refined unit cell parameters: $a = 8.7004(3)$, $b = 14.0971(6)$, $c = 8.0988(3)$ Å, $\beta = 90.356(3)°$ and $V = 993.30(7)$ Å^3.

2.3. Thermal Behavior of $Mg(BH_4)_2{\cdot}NH(CH_2CH_3)_2$

The thermal stability of $Mg(BH_4)_2{\cdot}NH(CH_2CH_3)_2$ (S1) was found to be 116 °C through a combination of thermogravimetric analysis and differential scanning calorimetry (see Figure 5a). Here, a continual exothermic event is observed, accompanied by mass loss. Furthermore, an endothermic event is observed at 83 °C without mass loss. This event is not initially observed in sample S2; however, a similar thermal stability is observed (see Figure 5b). Temperature-resolved synchrotron radiation powder X-ray diffraction of sample S1 shows decreasing crystallinity beginning at 75 °C, with diffraction peaks disappearing completely at 102 °C (see Figure 5c). These combined results suggest that the endothermic event in Figure 5a can be attributed to sample melting. Photos obtained during heating of the sample (see Figure S6 and Supporting Video S1) reveal melting of the sample in the temperature range of 72 to 86 °C. This process is also accompanied by gas release, observed as 'bubbling', which may be attributed to the boiling of diethylamine (T_{bp} = 55 °C). A second heating experiment was performed on S2, in which the sample was heated to 100 °C twice (see Figure S5). The sample shows no sign of melting on the second heating and remains a loose powder upon cooling. This suggests that a melt stabilization effect is present, like that of the $Mg(BH_4)_2{\cdot}1.6NH_3{-}MgO$ and $Mg(BH_4)_2{\cdot}1.6NH_3{-}Al_2O_3$ systems, in which nanoparticles prevent recrystallisation and stabilize an eutectic molten state at lower-than-expected temperatures and thereby cause high ionic conductivity and low activation energy below the melting point of the composites [15,25].

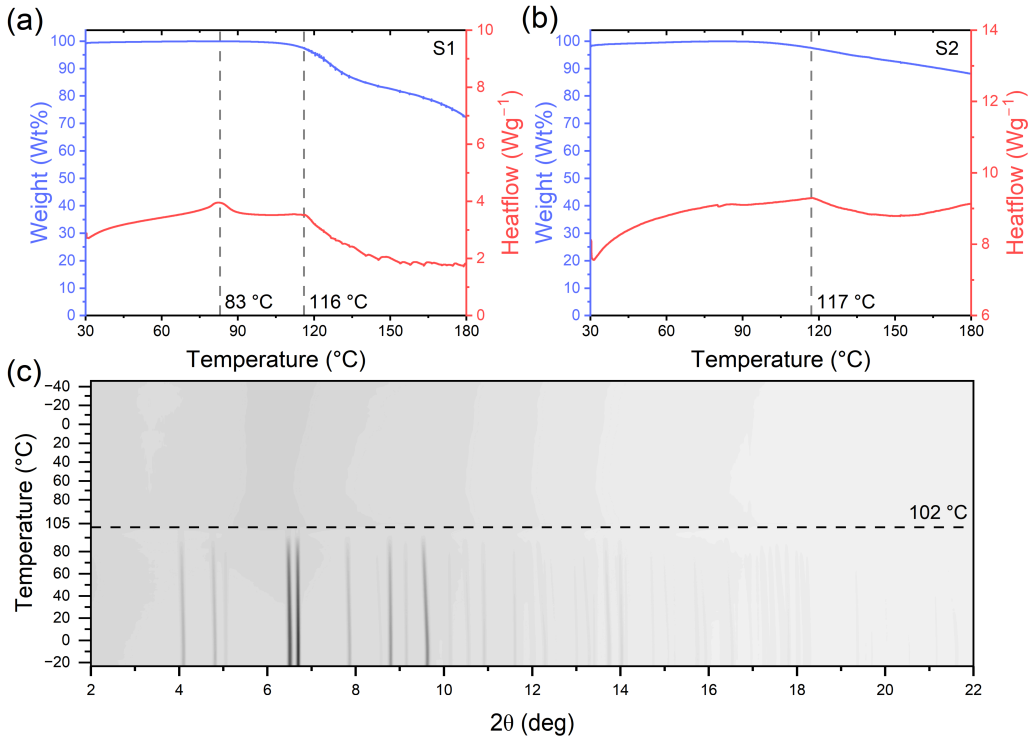


Figure 5. Thermal behavior of samples. Thermogravimetric analysis (blue) and differential scanning calorimetry (red) of (**a**) sample S1 and (**b**) sample S2 (heating rate 5 °C min^{-1}). (**c**) In situ diffraction measurement during heating of sample S1 (λ = 0.6199 Å).

2.4. Ionic Conductivity of $Mg(BH_4)_2{\cdot}NH(CH_2CH_3)_2$

It was not possible to measure the ionic conductivity of the pure sample (S1) due to the overall softness of the compound. However, after the addition of nanoparticles, the sample became powdery (S2) and could be cold pressed into a pellet. The sample composition remained the same upon pelletizing, showing no signs of decomposi-

tion (see Figure S7). It is noted that the addition of nanoparticles has previously been shown to both lower activation energy and change ionic conductivity [14,15,25,54–57]. Therefore, the conductivity presented here may not reflect the conductivity of the pure compound. After initial stabilization at room temperature, the ionic conductivity was measured in the temperature range −2 to 55 °C for sample S2 to stay below the melting point of 83 °C (see Figure S8). Previous studies of magnesium tetrahydridoborate derivatives reveal magnesium stripping and plating, in some cases >100 cycles, and no indications of any anionic or electronic conductivity have been reported [13,14,16]. Therefore, the ionic conductivity presented here is assigned to be magnesium ionic conductivity, although the magnesium transference number of S2 was not determined in this study. The ionic conductivity of S2 at −2 °C is high, $\sigma = 2.58 \times 10^{-6}$ S cm^{-1}, and increases to $\sigma = 2.01 \times 10^{-4}$ S cm^{-1} at 55 °C (see Figure 6a).

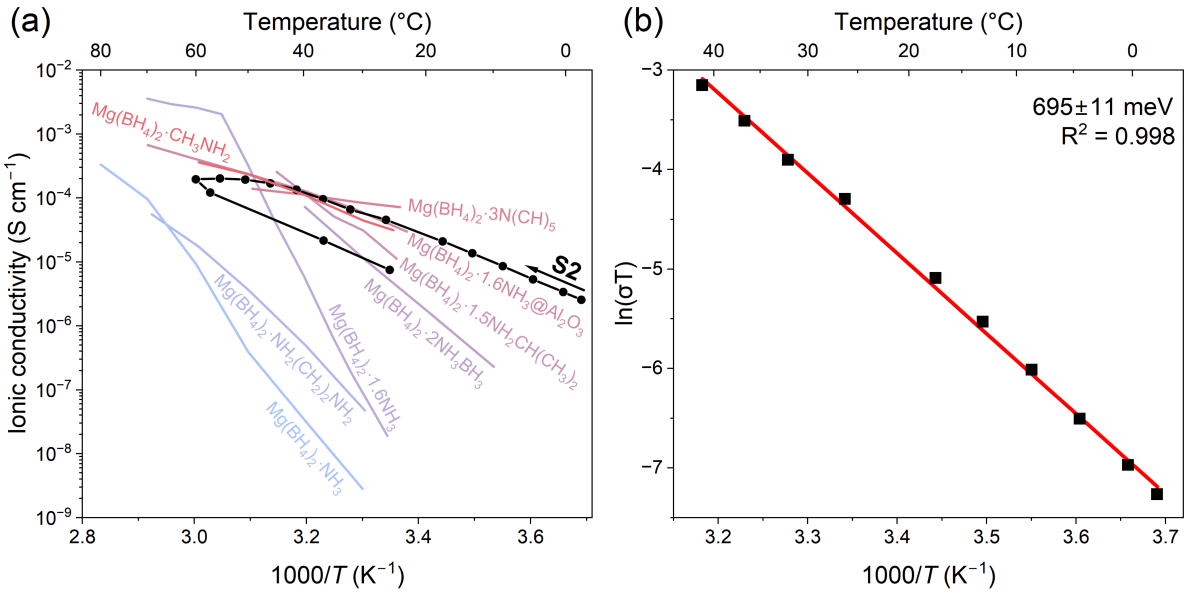


Figure 6. Ionic conductivity of sample S2. (**a**) Ionic conductivity of sample S2 compared to other known Mg^{2+} conductors [13–15,17,21,25,27]. (**b**) Fit of ion conductivity data point and resulting activation energy within the stable region.

The low-temperature conductivity is higher than that of the similar systems $Mg(BH_4)_2 \cdot NH_2CH_3$ and $Mg(BH_4)_2 \cdot 1.5NH_2CH(CH_3)_2$ (see Figure 6a). Compared to these, $NH(CH_2CH_3)_2$ may provide more flexibility than NH_2CH_3 due to the larger regions of weak dispersion interactions, while the separation of the $-CH_2CH_3$ moieties can provide more metastable intermediate states that promote ionic conductivity than the more rigid $NH_2CH(CH_3)_2$ [13,14]. The activation energy was found to be 695 ± 11 meV in the temperature range −2 to 40 °C (see Figure 6b).

The ionic conductivity of sample S2 was measured one month after the synthesis. The EIS data were measured during heating from −2 to 60 °C and during cooling at 57, 36 and 25 °C. As the sample is heated above 40 °C, the ionic conductivity deviates from linearity, suggesting a gradual change in mechanism for cationic migration possibly owing to changes within the sample (see Figure 6a). However, it is noted that no changes were observed in this temperature range in the thermal analysis results seen in Figures 5 and S6.

To further shed light on the cationic conductivity, EIS data were measured for sample S2 again, after ~18 months of storage in an argon-filled glovebox. These EIS data were measured in the temperature range 3–36 °C during three heating and cooling cycles; see Figure S9. The conductivity is very stable during these three thermal cycles and reveals the highest value, $\sigma = 5.8 \times 10^{-6}$ S cm^{-1} at 36 °C, and the lowest value, $\sigma = 5.1 \times 10^{-7}$ S cm^{-1}

at 3 °C. The average activation energy for cationic migration using all data presented in Figure S9 is $E_A = 609 \pm 14$ meV, which compares well to the activation energy observed for the data measured one month after the synthesis of sample S2.

However, comparing these measurements with the original conductivity data obtained one month after synthesis (see Figure S10) reveals that the conductivity has decreased more than an order of magnitude after drying the sample at RT for 18 months. A similar reduction in cationic conductivity is also observed for $Mg(BH_4)_2{\cdot}NH_2CH_3$ [13]. To further investigate the thermal stability of S2 after 18 months of storage, a pellet (Ø5 mm, pressed at 1 GPa) was preheated to 90 °C (in argon for 30 min). Then the cationic conductivity was measured using EIS; see Figure S11. Initially, the sample had conductivity comparable to the untreated sample; however, upon heating to 60 °C, the conductivity decreased drastically. This is possibly indicative of a small loss of diethylamine over an extended period, which changes the sample (S2) composition and thereby the conductivity.

Overall, these results represent a high level of performance for an inorganic solid-state magnesium ionic conductor and have the potential to enable cycling of a magnesium metal battery at or below room temperature [16].

3. Materials and Methods

3.1. Synthesis

The synthesis of mono-diethylamine magnesium tetrahydridoborate, $Mg(BH_4)_2{\cdot}NH(CH_3CH_2)_2$, starts with the preparation of the precursor, MgH_2. MgH_2 was synthesized by exposing magnesium powder (10 g, ~0.412 mol, sieved to 325 mesh) to H_2 at a pressure of 80 bar in a hermetically sealed pressure tube and subsequently heated to 400 °C for 12 h. MgH_2 was produced following reaction (1), where H_2 was added periodically to maintain a pressure of 80 bar.

$$Mg(s) + H_2(g) \xrightarrow{400\ ^\circ C,\quad p(H_2)\,=\,80bar} MgH_2(s) \tag{1}$$

Freshly synthesized MgH_2 (5 g, ~0.190 mol) was suspended in 50 mL anhydrous toluene. Dimethylsulphide borane complex, $H_3B{\cdot}S(CH_3)_2$ (50 mL, 10 M), was subsequently added slowly under stirring to yield a stoichiometric excess of ~30%. The mixture was heated to 40 °C and allowed to react for 7 days under stirring. Following reaction (2), $Mg(BH_4)_2{\cdot}½S(CH_3)_2$ solidified and precipitated along with unreacted components such as MgH_2 and potentially MgO.

$$MgH_2(s) + 2(CH_3)_2S{\cdot}BH_3(l) \xrightarrow{40\ ^\circ C} Mg(BH_4)_2{\cdot}{}^1\!/_2S(CH_3)_2(s) + {}^3\!/_2S(CH_3)_2(l) \tag{2}$$

The residual liquid was removed by filtration, and the solid was subsequently washed three times with anhydrous toluene. The solid was dried at room temperature (RT) while under dynamic vacuum for 1 h. To remove unreacted MgH_2, $Mg(BH_4)_2{\cdot}½S(CH_3)_2$ was dissolved in 100 mL diethyl ether. After filtration, the solution was evaporated using a rotary evaporator, producing a thick, transparent oil. Under vacuum, the oil was heated to 140 °C overnight, resulting in solid α-$Mg(BH_4)_2$ powder, which will act as the secondary precursor.

For the gas-mediated coordination between diethylamine ($NH(CH_2CH_3)_2$) and $Mg(BH_4)_2$, a custom, in-house manufactured twin-chamber reaction tube with two vertical tubes joined near the top by a hollow bridge was required. One chamber was filled with $Mg(BH_4)_2$ powder (200 mg, 3.71 mmol), and the other chamber was filled with 2 mL anhydrous diethylamine; see the synthesis schematic, Figure 1. Gentle heating was applied to the chamber containing diethylamine while stirring the $Mg(BH_4)_2$ powder. The increase in coordinated ligand was followed by continuous NMR measurements. This included extraction of the powder, collecting an NMR sample, and setting up the synthesis once again, iteratively, if needed.

The extracted product was a sticky solid (S1). To mechanically stabilize sample S1, Al_2O_3 nanoparticles (60 wt%, 13 nm) were added and homogenized using a mortar and pestle (S2), as ball milling was found to result in decomposition of the sample.

3.2. Powder X-Ray Diffraction

In-house powder X-ray diffraction (PXRD) data were collected on a Rigaku SmartLab diffractometer with a Cu anode (Cu Kα radiation, $\lambda = 1.54056$ Å) at RT. In situ temperature-resolved synchrotron radiation X-ray powder diffraction (SR PXRD) data were collected at the DanMAX beamline at MAXIV in Lund, Sweden ($\lambda = 0.61992$ Å).

3.3. Structure Solution and Refinement

Structural solution and refinement were performed using the software FOX (2024.1) and FullProf (5.10), respectively [58,59]. The BH_4^- and $NH(CH_3CH_2)_2$ groups were treated as rigid bodies in FOX while simulating. The structure was further refined with distance constraints in FullProf. The background was described by linear interpolation between selected points, while Pseudo-Voigt profile functions were used to fit the diffraction peaks.

3.4. Thermal Analysis

Thermogravimetric analysis and differential scanning calorimetry were measured using a PerkinElmer STA 6000. Each sample (approx. 5 mg) was placed in an Al_2O_3 crucible and heated in the temperature range of 30 to 180 °C ($\Delta T/\Delta t = 5$ °C/min) with an argon purge rate of 30 mL/min.

3.5. Liquid-State ^{1}H NMR and ^{11}B Nuclear Magnetic Resonance Spectroscopy

Liquid-state ^{1}H NMR and ^{11}B nuclear magnetic resonance (NMR) spectroscopy measurements were performed on a Bruker Ascend 400 MHz spectrometer equipped with a ^{1}H−^{13}C−^{15}N 5 mm TXI liquid-state probe. A rotational frequency of $\nu_R = 10.0$ kHz and a 0.5 µs excitation pulse ($\gamma B_1/2\pi = 58$ kHz) were used during the measurements. Deuterated dimethyl sulfoxide was used to dissolve the samples in NMR tubes before measuring.

A relaxation experiment on S1 was performed to ensure full relaxation of diethylamine when determining the sample composition. As the ^{1}H NMR measurements were conducted with a scan delay of 1 second, determination of the sample compositions should account for incomplete relaxation. The relaxation experiment was performed by increasing the scan delay τ on several measurements on the same NMR sample. The intensity was plotted and fitted to the general solution to the Bloch equation; see Equation (S1) and Figure S1. The deviation in intensity gathered at $\tau = 1$ s vs. intensity gathered at full relaxation could be determined. This was used to account for incomplete relaxation when determining the sample composition.

3.6. Fourier Transform Infrared Spectroscopy

Fourier transform infrared spectroscopy (FT-IR) was measured with a Spectrum Two FT-IR Spectrometer from PerkinElmer equipped with a $LiTaO_3$ universal attenuated total reflectance (UATR) detector. An average of 8 scans with a spectral resolution of 4 cm^{-1} was collected in the range of 500–4000 cm^{-1}.

3.7. Electrochemical Characterization

Electrochemical impedance spectroscopy (EIS) data were collected using a BioLogic MTZ-35 impedance analyser equipped with a custom high-temperature sample holder made in-house. The electrolytes were pressed into 5 mm diameter pellets with a thickness of ~1 mm under the pressure of 1 GPa for five minutes. Impedance data were measured in

a frequency range from 1.1 MHz to 1.1 Hz with an amplitude of 10 mV in the temperature range from −2 to 55 °C. A time-dependent evolution of the ionic conductivity was observed for other metal tetrahydridoborates with neutral ligands due to the relaxation of the pellet after compression [40]. To prevent this, EIS data were measured every 30 min at RT until a stable impedance was achieved before initializing the measurements at elevated temperatures.

Measurements were performed using a symmetric cell configuration with in-house machined Mo ionic-blocking electrodes, Mo| S2 |Mo. An equivalent circuit, $Q_1/(R_1 + Q2)$, was used to fit the obtained Nyquist plots. R_1 and Q_1 relate to the ionic conduction within the electrolyte. Q_2 is assigned to the capacitive charge buildup on the Mo electrodes.

3.8. Density Functional Theory Calculations

Density functional theory (DFT) calculations were performed using the GPAW code (version 26.7.0), using the experimentally determined crystal structure of $Mg(BH_4)_2 \cdot NH(CH_2CH_3)_2$ as the starting geometry, with the experimental lattice parameters and unit-cell dimensions kept fixed during structural optimization. The atomic positions were subsequently relaxed while maintaining the experimental unit cell.

The Perdew–Burke–Ernzerhof (PBE) exchange–correlation functional was employed together with a plane-wave basis set using a kinetic-energy cutoff of 500 eV. Brillouin-zone sampling was performed using a 2 × 2 × 2 Monkhorst–Pack k-point mesh. Dispersion interactions were included using the D3 dispersion correction with Becke–Johnson damping (PBE-D3(BJ)).

The atomic structure was optimized using the BFGS algorithm until the maximum residual force on any atom was below 0.02 eV $Å^{-1}$. During the optimization, the lattice parameters and unit-cell angles were constrained to their experimentally determined values, while all atomic coordinates were allowed to relax.

4. Conclusions

Magnesium tetrahydridoborate derivatives have shown high ionic conductivities owing to flexible inorganic structures built from weak interactions such as dispersion interactions between organic moieties and dihydrogen bonds, $B–H^{\delta-}\cdots{}^{+\delta}H–N$. Here, the synthesis methods, structure and thermal properties of mono-diethylamine magnesium tetrahydridoborate, $Mg(BH_4)_2NH(CH_2CH_3)_2$, as well as the ionic conductivity of the composite $Mg(BH_4)_2 \cdot NH(CH_2CH_3)_2$−60 wt% Al_2O_3, are reported. The new compound, $Mg(BH_4)_2 \cdot NH(CH_2CH_3)_2$, crystallizes in space group $P2_1/c$ with unit cell parameters $a = 8.700(3)$, $b = 14.097(6)$, $c = 8.099(3)$ Å, $\beta = 90.36(3)°$ and $V = 993.31(7)$ $Å^3$ at $T = 22$ °C. The structure consists of 1D zig-zag chains that are held together by dispersive forces. The compound was found to melt at 83 °C and to start decomposing at 116 °C. The sample was found to be soft and malleable, which necessitated the addition of inert, insulating Al_2O_3 nanoparticles (13 nm) to increase mechanical stability. This has the apparent effect of suppressing recrystallisation while maintaining the same thermal stability. The composite $Mg(BH_4)_2 \cdot NH(CH_2CH_3)_2$−60 wt% Al_2O_3 has an ionic conductivity $\sigma = 2.58 \times 10^{-6}$ S cm^{-1} at −2 °C increasing to $\sigma = 2.01 \times 10^{-4}$ S cm^{-1} at 55 °C with an activation energy of 695 ± 11 meV. However, long-term storage at RT (for 1.5 years) has a stabilizing effect so that the conductivity is stable during several consecutive heating and cooling cycles, but overall decreases by more than one order of magnitude as compared to the freshly prepared sample. The high conductivity can be assigned to a relatively open one-dimensional structure similar to several other magnesium tetrahydridoborate derivatives with record-high ionic conductivity. This compound, $Mg(BH_4)_2 \cdot NH(CH_2CH_3)_2$, has a relatively large organic moiety compared to other derivatives in this class of compounds, which contributes

to a larger fraction of weak dispersion interactions. However, the large organic moiety also contributes to the softness of this compound and the low melting point. These results show a promising avenue towards high-energy-density magnesium metal batteries.

Supplementary Materials: The following supporting information can be downloaded at https://www.mdpi.com/article/10.3390/inorganics14110279/s1. Video S1: Melting of the electrolyte; Figure S1: liquid-phase ^{1}H-NMR and ^{11}B-NMR of samples S1 and S2; Figure S2: ^{1}H-NMR relaxation experiment data performed on sample S1; Figure S3: liquid-phase ^{1}H-NMR and ^{11}B-NMR of sample S3; Figure S4: structural optimization; Figure S5: thermal behaviour of sample S2 on repeated heating; Figure S6: heating of sample S1 under inert atmosphere; Figure S7: liquid-state NMR of pelletized sample S2; Figure S8: Nyquist plots of sample S2; Figure S9: ionic conductivity of S2 after long-term storage; Figure S10: long-term stability; Figure S11: preheating of S2.

Author Contributions: Conceptualization, O.G.Ø. and T.R.J.; methodology, O.G.Ø. and L.R.K.; software, O.G.Ø. and L.R.K.; formal analysis, O.G.Ø. and L.R.K.; investigation, O.G.Ø. and L.R.K.; resources, T.R.J.; data curation, O.G.Ø. and L.R.K.; writing, O.G.Ø., L.R.K. and T.R.J.; visualization, O.G.Ø. and L.R.K.; supervision, L.R.K. and T.R.J.; project administration, T.R.J.; funding acquisition, T.R.J. All authors have read and agreed to the published version of the manuscript.

Funding: This research was funded by the Independent Research Fund Denmark for Technology and Production grant number DFF-0217-00327B.

Data Availability Statement: The raw data supporting the conclusions of this article will be made available by the authors on request.

Acknowledgments: Affiliation with Aarhus University's Materials Research Cluster, AU Materials, is gratefully acknowledged. T.R.J. is grateful for the association with the Distinguished Foreign Scientist Workstation for Hydrogen Energy Storage (GZS2025006) led by project leader Baozhong Liu. We acknowledge the MAX IV Laboratory for beamtime on the DanMAX beamline under proposal 20252178. Research conducted at MAX IV, a Swedish national user facility, is supported by Vetenskapsrådet (Swedish Research Council, VR) under contract 2018-07152, Vinnova (Swedish Governmental Agency for Innovation Systems) under contract 2018-04969, and Formas under contract 2019-02496. DanMAX is funded by the NUFI grant no. 4059-00009B.

Conflicts of Interest: The authors declare no conflicts of interest.

Abbreviations

The following abbreviations are used in this manuscript:

NMR	Nuclear Magnetic Resonance
FT-IR	Fourier transform infrared spectroscopy
PXRD	Powder X-ray diffraction
EIS	Electrochemical impedance spectroscopy
DFT	Density functional theory
PBE	Perdew–Burke–Ernzerhof

References

1. Dunn, B.; Kamath, H.; Tarascon, J.-M. Electrical Energy Storage for the Grid: A Battery of Choices. *Science* **2011**, *334*, 928–935. [CrossRef] [PubMed]
2. Broom, D.P.; Allendorf, M.D.; Autrey, T.; Baricco, M.; Bellosta von Colbe, J.; Bowden, M.E.; Buckley, C.E.; Chen, P.; Cuevas, F.; Deledda, S.; et al. Hydrogen-Based Materials for Energy Storage and Conversion. *Nat. Rev. Clean. Technol.* **2026**, *2*, 512–533. [CrossRef]
3. Allendorf, M.D.; Stavila, V.; Snider, J.L.; Witman, M.; Bowden, M.E.; Brooks, K.; Tran, B.L.; Autrey, T. Challenges to Developing Materials for the Transport and Storage of Hydrogen. *Nat. Chem.* **2022**, *14*, 1214–1223. [CrossRef] [PubMed]
4. Alhmoud, L.; Bani Fayyad, M.; Tamimi, M.; Albataineh, Z. Performance Evaluation of Grid-Forming Battery Energy Storage Systems for Stability Enhancement in Solar PV Plants. *Sci. Rep.* **2026**, *16*, 26925. [CrossRef] [PubMed]

5. Mousavian, S.M.H.; Bautin, V.A. Rechargeable Magnesium Batteries: Overcoming Challenges for High-Efficiency Energy Applications. *J. Energy Storage* **2025**, *126*, 117079. [CrossRef]
6. Lin, L.; Qin, K.; Hu, Y.; Li, H.; Huang, X.; Suo, L.; Chen, L. A Better Choice to Achieve High Volumetric Energy Density: Anode-Free Lithium-Metal Batteries. *Adv. Mater.* **2022**, *34*, e2110323. [CrossRef] [PubMed]
7. Kim, H.S.; Arthur, T.S.; Allred, G.D.; Zajicek, J.; Newman, J.G.; Rodnyansky, A.E.; Oliver, A.G.; Boggess, W.C.; Muldoon, J. Structure and Compatibility of a Magnesium Electrolyte with a Sulphur Cathode. *Nat. Commun.* **2011**, *2*, 427. [CrossRef] [PubMed]
8. Wang, L.; Riedel, S.; Drews, J.; Zhao-Karger, Z. Recent Developments and Future Prospects of Magnesium–Sulfur Batteries. *Front. Batter. Electrochem.* **2024**, *3*, 1358199. [CrossRef]
9. Bieker, G.; Küpers, V.; Kolek, M.; Winter, M. Intrinsic Differences and Realistic Perspectives of Lithium-Sulfur and Magnesium-Sulfur Batteries. *Commun. Mater.* **2021**, *2*, 37. [CrossRef]
10. Bracamonte, M.V.; Vizintin, A.; Kapun, G.; Cometto, F.; Bitenc, J.; Randon-Vitanova, A.; Gaberšček, M.; Dominko, R. Surface Film Formation on Mg Electrode Containing Magnesium Polysulfides in TFSI-Based Electrolytes. *J. Power Sources* **2023**, *555*, 232367. [CrossRef]
11. Sau, K.; Takagi, S.; Ikeshoji, T.; Kisu, K.; Sato, R.; dos Santos, E.C.; Li, H.; Mohtadi, R.; Orimo, S. Unlocking the Secrets of Ideal Fast Ion Conductors for All-Solid-State Batteries. *Commun. Mater.* **2024**, *5*, 122. [CrossRef]
12. Brinckerhoff, A.; Fang, H. Emerging Developments of Inorganic Magnesium Solid-State Electrolytes. *PRX Energy* **2026**, *5*, 027001. [CrossRef]
13. Amdisen, M.B.; Grinderslev, J.B.; Skov, L.N.; Jensen, T.R. Methylamine Magnesium Borohydrides as Electrolytes for All-Solid-State Magnesium Batteries. *Chem. Mater.* **2023**, *35*, 1440–1448. [CrossRef]
14. Kristensen, L.G.; Amdisen, M.B.; Skov, L.N.; Jensen, T.R. Fast Magnesium Ion Conducting Isopropylamine Magnesium Borohydride Enhanced by Hydrophobic Interactions. *Phys. Chem. Chem. Phys.* **2022**, *24*, 18185–18197. [CrossRef] [PubMed]
15. Yan, Y.; Grinderslev, J.B.; Jørgensen, M.; Skov, L.N.; Skibsted, J.; Jensen, T.R. Ammine Magnesium Borohydride Nanocomposites for All-Solid-State Magnesium Batteries. *ACS Appl. Energy Mater.* **2020**, *3*, 9264–9270. [CrossRef]
16. Skov, L.N.; Grinderslev, J.B.; Rosenkranz, A.; Lee, Y.-S.; Jensen, T.R. Towards Solid-State Magnesium Batteries: Ligand-Assisted Superionic Conductivity. *Batter. Supercaps* **2022**, *5*, e202200163. [CrossRef]
17. Kisu, K.; Kim, S.; Inukai, M.; Oguchi, H.; Takagi, S.; Orimo, S. Magnesium Borohydride Ammonia Borane as a Magnesium Ionic Conductor. *ACS Appl. Energy Mater.* **2020**, *3*, 3174–3179. [CrossRef]
18. Černý, R.; Filinchuk, Y.; Hagemann, H.; Yvon, K. Magnesium Borohydride: Synthesis and Crystal Structure. *Angew. Chem. Int. Ed.* **2007**, *46*, 5765–5767. [CrossRef] [PubMed]
19. Webb, C.J.; Humphries, T.D.; Teprovich, J.A.; Polanski, M.; Heere, M.; Li, H.-W.; Felderhoff, M.; Filinchuk, Y.; Dornheim, M.; Paskevicius, M.; et al. Diverse Hydrogen Chemistry with Perspectives for Energy Storage. *Chem. Commun.* **2026**, *62*, 4477–4495. [CrossRef] [PubMed]
20. Li, Z.; Diemant, T.; Meng, Z.; Xiu, Y.; Reupert, A.; Wang, L.; Fichtner, M.; Zhao-Karger, Z. Establishing a Stable Anode–Electrolyte Interface in Mg Batteries by Electrolyte Additive. *ACS Appl. Mater. Interfaces* **2021**, *13*, 33123–33132. [CrossRef] [PubMed]
21. Roedern, E.; Kühnel, R.-S.; Remhof, A.; Battaglia, C. Magnesium Ethylenediamine Borohydride as Solid-State Electrolyte for Magnesium Batteries. *Sci. Rep.* **2017**, *7*, 46189. [CrossRef] [PubMed]
22. Golub, I.E.; Heere, M.; Gounaris, V.; Li, X.; Steenhaut, T.; Wang, J.; Robeyns, K.; Li, H.-W.; Dovgaliuk, I.; Ikeda, K.; et al. Structural Insight into the Magnesium Borohydride—Ethylenediamine Solid-State Mg-Ion Electrolyte System. *Dalton Trans.* **2023**, *52*, 2404–2411. [CrossRef] [PubMed]
23. Burankova, T.; Roedern, E.; Maniadaki, A.E.; Hagemann, H.; Rentsch, D.; Lodziana, Z.; Battaglia, C.; Remhof, A.; Embs, J.P. Dynamics of the Coordination Complexes in a Solid-State Mg Electrolyte. *J. Phys. Chem. Lett.* **2018**, *9*, 6450–6455. [CrossRef] [PubMed]
24. Higashi, S.; Miwa, K.; Aoki, M.; Takechi, K. A Novel Inorganic Solid State Ion Conductor for Rechargeable Mg Batteries. *Chem. Commun.* **2014**, *50*, 1320–1322. [CrossRef] [PubMed]
25. Yan, Y.; Grinderslev, J.B.; Burankova, T.; Wei, S.; Embs, J.P.; Skibsted, J.; Jensen, T.R. Fast Room-Temperature Mg^{2+} Conductivity in $Mg(BH_4)_2{\cdot}1.6NH_3$–Al_2O_3 Nanocomposites. *J. Phys. Chem. Lett.* **2022**, *13*, 2211–2216. [CrossRef] [PubMed]
26. Kristensen, L.G.; Grinderslev, J.B.; Amdisen, M.B.; Jensen, T.R. Ligand Substitution as a Strategy to Tailor Cationic Conductivity in All-Solid-State Batteries. *Commun. Mater.* **2024**, *5*, 107. [CrossRef]
27. Grinderslev, J.B.; Jensen, T.R. Magnesium Borohydride Pyridine Derivatives as Solid Electrolytes for All-Solid-State Batteries. *J. Mater. Chem. A* **2025**, *13*, 15810–15817. [CrossRef]
28. Grinderslev, J.B.; Skov, L.N.; Kristensen, L.R.; Jensen, T.R. Advancing Solid-State Calcium Batteries: Achieving Fast Ionic Conductivity at Near Ambient Conditions in Calcium Hydridoborates. *Angew. Chem. Int. Ed.* **2025**, *64*, e202510493. [CrossRef] [PubMed]

29. Yan, Y.; Kühnel, R.-S.; Remhof, A.; Duchêne, L.; Reyes, E.C.; Rentsch, D.; Łodziana, Z.; Battaglia, C. A Lithium Amide-Borohydride Solid-State Electrolyte with Lithium-Ion Conductivities Comparable to Liquid Electrolytes. *Adv. Energy Mater.* **2017**, *7*, 1700294. [CrossRef]
30. Brighi, M.; Murgia, F.; Łodziana, Z.; Schouwink, P.; Wołczyk, A.; Cerny, R. A Mixed Anion Hydroborate/Carba-Hydroborate as a Room Temperature Na-Ion Solid Electrolyte. *J. Power Sources* **2018**, *404*, 7–12. [CrossRef]
31. Sadikin, Y.; Brighi, M.; Schouwink, P.; Černý, R. Superionic Conduction of Sodium and Lithium in Anion-Mixed Hydroborates $Na_3BH_4B_{12}H_{12}$ and $(Li_{0.7}Na_{0.3})_3BH_4B_{12}H_{12}$. *Adv. Energy Mater.* **2015**, *5*, 1501016. [CrossRef]
32. Gigante, A.; Duchêne, L.; Moury, R.; Pupier, M.; Remhof, A.; Hagemann, H. Direct Solution-Based Synthesis of $Na_4(B_{12}H_{12})(B_{10}H_{10})$ Solid Electrolyte. *ChemSusChem* **2019**, *12*, 4832–4837. [CrossRef] [PubMed]
33. Sadikin, Y.; Schouwink, P.; Brighi, M.; Łodziana, Z.; Černý, R. Modified Anion Packing of $Na_2B_{12}H_{12}$ in Close to Room Temperature Superionic Conductors. *Inorg. Chem.* **2017**, *56*, 5006–5016. [CrossRef] [PubMed]
34. Jepsen, L.H.; Ley, M.B.; Lee, Y.-S.; Cho, Y.W.; Dornheim, M.; Jensen, J.O.; Filinchuk, Y.; Jørgensen, J.-E.; Besenbacher, F.; Jensen, T.R. Boron–Nitrogen Based Hydrides and Reactive Composites for Hydrogen Storage. *Mater. Today* **2014**, *17*, 129–135. [CrossRef]
35. Asakura, R.; Duchêne, L.; Kühnel, R.-S.; Remhof, A.; Hagemann, H.; Battaglia, C. Electrochemical Oxidative Stability of Hydroborate-Based Solid-State Electrolytes. *ACS Appl. Energy Mater.* **2019**, *2*, 6924–6930. [CrossRef]
36. Nguyen, T.P.T.; Gao, W.; Conghaile, P.Ó.; Humphries, T.D.; Buckley, C.E.; Paskevicius, M. Room Temperature One-Pot Synthesis of $M_3B_{24}H_{23}$ (M = Na and Li) and Their Investigation as Solid-State Electrolytes. *J. Electrochem. Soc.* **2026**, *173*, 150501. [CrossRef]
37. Braun, H.; Battaglia, C.; Remhof, A. Hydridoborate Solid Electrolytes: Opportunities and Challenges. *Chem. Commun.* **2026**, *62*, 10553–10565. [CrossRef] [PubMed]
38. Braun, H.; Łodziana, Z.; Battaglia, C.; Remhof, A. Electrochemical Reductive Stability of Lithium Hydridoborate Solid-State Electrolytes. *J. Mater. Sci. Mater. Energy* **2026**, *2*, 2. [CrossRef]
39. Faurskov, T.S.S.; Grinderslev, J.B.; Kristensen, L.R.; Jensen, T.R. Stabilization of the Highly Conductive Sodium Solid Electrolyte *Ht*-$NaCB_9H_{10}$ Using High-Energy Ball Milling. *ACS Mater. Lett.* **2026**, *8*, 2905–2911. [CrossRef]
40. Grinderslev, J.B.; Skov, L.N.; Andreasen, J.G.; Ghorwal, S.; Skibsted, J.; Jensen, T.R. Methylamine Lithium Borohydride as Electrolyte for All-Solid-State Batteries. *Angew. Chem. Int. Ed.* **2022**, *61*, e202203484. [CrossRef] [PubMed]
41. Asakura, R.; Łodziana, Z.; Grissa, R.; Rentsch, D.; Battaglia, C.; Remhof, A. Unveiling Solid-State Electrochemical Oxidation of $LiBH_4$ and $Li_2B_{12}H_{12}$ for High-Voltage All-Solid-State Batteries. *ACS Appl. Energy Mater.* **2025**, *8*, 9637–9645. [CrossRef]
42. Mohtadi, R.; Matsui, M.; Arthur, T.S.; Hwang, S.-J. Magnesium Borohydride: From Hydrogen Storage to Magnesium Battery. *Angew. Chem. Int. Ed. Engl.* **2012**, *51*, 9780–9783. [CrossRef] [PubMed]
43. Wang, D.; Gao, X.; Chen, Y.; Jin, L.; Kuss, C.; Bruce, P.G. Plating and Stripping Calcium in an Organic Electrolyte. *Nat. Mater.* **2018**, *17*, 16–20. [CrossRef] [PubMed]
44. Biria, S.; Pathreeker, S.; Genier, F.S.; Li, H.; Hosein, I.D. Plating and Stripping Calcium at Room Temperature in an Ionic-Liquid Electrolyte. *ACS Appl. Energy Mater.* **2020**, *3*, 2310–2314. [CrossRef]
45. Kisu, K.; Kim, S.; Shinohara, T.; Zhao, K.; Züttel, A.; Orimo, S. Monocarborane Cluster as a Stable Fluorine-Free Calcium Battery Electrolyte. *Sci. Rep.* **2021**, *11*, 7563. [CrossRef] [PubMed]
46. Zhao, W.; Liu, Y.; Zhao, X.; Pan, Z.; Chen, J.; Zheng, S.; Qu, L.; Yang, X. Chloride-Free Electrolytes for High-Voltage Magnesium Metal Batteries: Challenges, Strategies, and Perspectives. *Chem.—A Eur. J.* **2023**, *29*, e202203334. [CrossRef] [PubMed]
47. Shao, Y.; Liu, T.; Li, G.; Gu, M.; Nie, Z.; Engelhard, M.; Xiao, J.; Lv, D.; Wang, C.; Zhang, J.-G.; et al. Coordination Chemistry in Magnesium Battery Electrolytes: How Ligands Affect Their Performance. *Sci. Rep.* **2013**, *3*, 3130. [CrossRef] [PubMed]
48. Su, S.; NuLi, Y.; Wang, N.; Yusipu, D.; Yang, J.; Wang, J. Magnesium Borohydride-Based Electrolytes Containing 1-Butyl-1-Methylpiperidinium Bis(Trifluoromethyl Sulfonyl)Imide Ionic Liquid for Rechargeable Magnesium Batteries. *J. Electrochem. Soc.* **2016**, *163*, D682. [CrossRef]
49. Movsesyan, K.; Prager, M.A.; Vergara-Reyes, E.; Ward, P.A.; Jensen, C.M.; Teprovich, J.A. Partially Dehydrogenated $Mg(BH_4)_2$-Pyrrolidine Complex as a Magnesium Battery Electrolyte. *Ionics* **2026**, *32*, 10021–10031. [CrossRef]
50. Prus, A.; Wu, H.; Zhou, W.; Bhandarkar, A.; Teprovich, J.A., Jr.; Fijalkowski, K.J.; Talin, A.A.; Stavila, V. Phase Behavior, Structural Dynamics, and Ionic Conductivity in Perhalogenated Lithium Closo-Dodecaborates. *Chem. Mater.* **2026**, *38*, 5960–5972. [CrossRef]
51. Green, M.; Kaydanik, K.; Orozco, M.; Hanna, L.; Marple, M.A.T.; Fessler, K.A.S.; Jones, W.B.; Stavila, V.; Ward, P.A.; Teprovich, J.A., Jr. Closo-Borate Gel Polymer Electrolyte with Remarkable Electrochemical Stability and a Wide Operating Temperature Window. *Adv. Sci.* **2022**, *9*, 2106032. [CrossRef] [PubMed]
52. Kristensen, L.G.; Amdisen, M.B.; Andersen, M.; Jensen, T.R. Synthesis, Structure and Mg^{2+} Ionic Conductivity of Isopropylamine Magnesium Borohydride. *Inorganics* **2023**, *11*, 17. [CrossRef]
53. Yan, Y.; Dononelli, W.; Jørgensen, M.; Grinderslev, J.B.; Lee, Y.-S.; Cho, Y.W.; Černý, R.; Hammer, B.; Jensen, T.R. The Mechanism of Mg^{2+} Conduction in Ammine Magnesium Borohydride Promoted by a Neutral Molecule. *Phys. Chem. Chem. Phys.* **2020**, *22*, 9204–9209. [CrossRef] [PubMed]

54. Gulino, V.; Barberis, L.; Ngene, P.; Baricco, M.; de Jongh, P.E. Enhancing Li-Ion Conductivity in $LiBH_4$-Based Solid Electrolytes by Adding Various Nanosized Oxides. *ACS Appl. Energy Mater.* **2020**, *3*, 4941–4948. [CrossRef]
55. Lambregts, S.F.H.; van Eck, E.R.H.; Ngene, P.; Kentgens, A.P.M. The Nature of Interface Interactions Leading to High Ionic Conductivity in $LiBH_4/SiO_2$ Nanocomposites. *ACS Appl. Energy Mater.* **2022**, *5*, 8057–8066. [CrossRef] [PubMed]
56. Blanchard, D.; Nale, A.; Sveinbjörnsson, D.; Eggenhuisen, T.M.; Verkuijlen, M.H.W.; Suwarno; Vegge, T.; Kentgens, A.P.M.; Jongh, P.E. de Nanoconfined $LiBH_4$ as a Fast Lithium Ion Conductor. *Adv. Funct. Mater.* **2015**, *25*, 184–192. [CrossRef]
57. de Kort, L.M.; Gulino, V.; de Jongh, P.E.; Ngene, P. Ionic Conductivity in Complex Metal Hydride-Based Nanocomposite Materials: The Impact of Nanostructuring and Nanocomposite Formation. *J. Alloys Compd.* **2022**, *901*, 163474. [CrossRef]
58. Favre-Nicolin, V.; Černý, R. FOX, 'free Objects for Crystallography': A Modular Approach to Ab Initio Structure Determination from Powder Diffraction. *J. Appl. Cryst.* **2002**, *35*, 734–743. [CrossRef]
59. Rodríguez-Carvajal, J. Recent Advances in Magnetic Structure Determination by Neutron Powder Diffraction. *Phys. B Condens. Matter* **1993**, *192*, 55–69. [CrossRef]

Disclaimer/Publisher's Note: The statements, opinions and data contained in all publications are solely those of the individual author(s) and contributor(s) and not of MDPI and/or the editor(s). MDPI and/or the editor(s) disclaim responsibility for any injury to people or property resulting from any ideas, methods, instructions or products referred to in the content.